Instability modes and transition of pulsatile stenotic flow: pulse-period dependence

By H. M. BLACKBURN[1] AND S. J. SHERWIN[2]

[1]CSIRO Manufacturing and Infrastructure Technology, PO Box 56, Highett, Vic 3190, Australia

[2]Department of Aeronautics, Imperial College London, South Kensington Campus, London, SW7 2AZ, UK

(Received 14 October 2005)

The instability modes arising within simple non-reversing pulsatile flows in a circular tube with a smooth axisymmetric constriction are examined using global Floquet stability analysis and direct numerical simulation. The sectionally averaged pulsatile flow is represented with one harmonic component superimposed on a time-mean flow. In prior work (Sherwin & Blackburn 2005) we identified a period-doubling absolute instability mechanism associated with alternating tilting of the vortex rings that are ejected out of the stenosis throat with each pulse. In this paper we show that while this is the primary instability mode for comparatively larger reduced velocities associated with long pulse periods (or low Womersley numbers), for lower reduced velocities that are associated with shorter pulse periods the primary instability typically manifests as azimuthal waves (Widnall instability modes) of low wavenumber that grow on each vortex ring. It is also shown that the shear layer of the steady axisymmetric flow is convectively unstable at still shorter temporal periods, and at Reynolds numbers well below the onset of the first three-dimensional absolute instability mode.

1. Introduction

Pulsatile flow in a straight tube with a smooth axisymmetric constriction provides an idealisation of vascular flow in a stenosed artery, where such occlusions are typically associated with atherosclerotic plaques. The close association between arterial disease and flow-related mechanisms (Caro, Fitz-Gerald & Schroter 1971) has motivated a number of studies of flow within both idealised and anatomically correct model stenoses as reviewed by Berger & Jou (2000).

Some of the ealiest investigations into stenotic transitional flows were undertaken experimentally in idealised axisymmetric stenotic tubes (Cassanova & Giddens 1978; Khalifa & Giddens 1981; Ahmed & Giddens 1983, 1984; Ojha, Cobbold, Johnston & Hummel 1989). The application of computational fluid dynamics has more recently made an impact, through numerical simulations of both idealised and anatomical geometries (Stroud, Berger & Saloner 2000; Long, Xu, Ramnarine & Hoskins 2001; Mallinger & Drikakis 2002; Stroud, Berger & Saloner 2002). This body of work has tended to consider either axisymmetric geometries or more complex anatomically derived geometries which cannot be readily reproduced. In contrast the complementary problem of a two-dimensional channel has been investigated in both symmetric and non-symmetric, yet idealised, configurations although even for the symmetric configuration the flow instabilities appear quite distinct to those which arise in axisymmetric geometries (Sobey &

Drazin 86; Pedley 2000; Mittal, Simmons & Najjar 2003; Pitt, Sherwin & Theofilis 2005). A very recent investigation (Varghese, Frankel & Fischer 2005) examines flow transition in a non-symmetric, idealised constricted tube.

In nearly all of the above studies, flow instability and transition to turbulence has been a common focus. Motivation is provided by the fact that under standard physiological conditions, arterial flows are usually considered to be laminar, although always unsteady and often with separation. However, in the case of a stenotic pipe flow, the increase in local Reynolds number due to the constriction and the introduction of an inflection point into the velocity profile downstream of the constriction can lead to flow transition.

Experimental studies of pulsatile stenotic flows with axisymmetric contractions have suggested that transition occurs a few pipe diameters downstream of the stenosis, does not always persist over the whole pulse cycle, and that flow relaminarises downstream. For example Ojha *et al.* (1989), in a flow-visualisation experiment with a 75%-occlusion stenosis, divided the post-stenotic flow into four zones. Zone I, reaching to three diameters downstream, is called the 'stable jet region', although some indication of wavy structure is observed on the jet front in this region; Zone II, spanning 3–4.5 diameters downstream, is called the 'transition region', where the waves become larger; in Zone III, the 'turbulent region', 4.5–7.5 diameters downstream, the front rapidly distorts; Zone IV, further downstream again, is labelled 'relaminarization'.

Experimental investigation and/or direct numerical simulation of turbulent flows does not necessarily provide a sound basis for understanding of the underlying instability mechanisms leading to transition. Insight into these mechanisms can often be obtained by the linearised stability analysis of a steady or time-periodic flow. For purely oscillatory flows in unconstricted straight tubes, instability mechanisms have been investigated by Yang & Yih (1977) and Akhavan, Kamm & Shapiro (1991). Recently, the present authors applied global Floquet analysis of the governing equations, linearised about a two-dimensional axisymmetric state which included the stenotic geometry, and coupled this with direct numerical simulation of transitional flows (Sherwin & Blackburn 2005). That work identified the instability modes and transition for both single- and two-harmonic pulsatile stenotic flow in the parameter range of time-averaged Reynolds number (based on mean flow and diameter) between 250 to 550 and non-dimensional pulse period (or equivalently reduced velocity) from 2.5 to 7.5. It was demonstrated that in the range of parameters investigated the transition to turbulence was initiated by a period-doubling instability of the vortex rings that are ejected from the stenosis during each pulsatile cycle. The transitional behaviour agrees in broad terms with the zonal categorization supplied by Ojha *et al.* (1989), although the specifics of the length scales were somewhat different. Another finding of our earlier work was that the extended jet shear layer which rolls up to form vortex rings can be susceptible to convective instability, which probably accounts for the wavy structures observed in Ojha *et al.*'s Zone I, and in the immediate post-stenotic regions of other experiments.

In the present work we return to the same theme, but provide a more systematic and expansive parametric study of the effect of pulse period on instability modes in single-harmonic (mean plus oscillatory) stenotic flow. In expanding the scope of the investigation we have now identified two different absolute instability mechanisms which can arise in pulsatile stenotic pipe flows: a period doubling instability and a short wavelength vortex core instability. Both are associated with the creation and transport of a new vortex ring during each pulse, which is a fundamental feature of pulsatile stenotic flow. On the other hand, in order to better study convective shear-layer instability we have concentrated on a parametric investigation of small harmonic perturbations of steady flow through

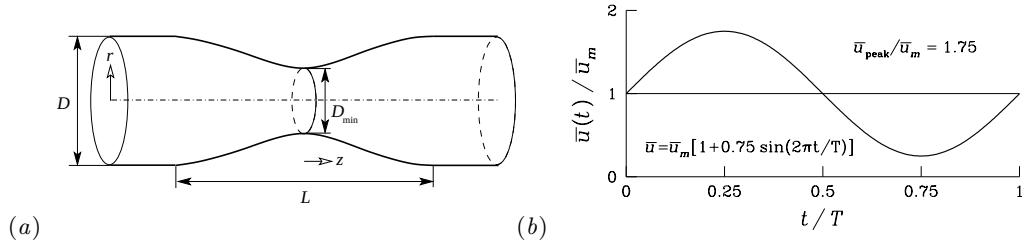

(*a*) (*b*)

FIGURE 1. (*a*) Stenosis geometry and (*b*) pulsatile flow waveform considered in this study.

our stenotic geometry, and demonstrate that its separated shear layer is susceptible to perturbations with high-frequency content.

1.1. *Problem definition and dimensionless groups*

The stenosis under investigation has a 50% diametral contraction with a smooth sinusiodal axial profile. Adoption of this level of occlusion (50% on diameter, 75% on area) is motivated by the observation that in clinical practice it is a level readily identified through ultrasound imaging, and has also been used in a number of other studies. The symmetry of the system means that a cylindrical coordinate system is the natural choice, and we locate the origin at the centre of the stenosis, as indicated in figure 1 (*a*). The axial profile of the stenosis is given by

$$r(z) = 0.5D_{\min} + 0.5(D - D_{\min})\sin^2(\pi z/L) \quad \text{over} \quad -0.5 \leqslant (z/L) < 0.5,$$

where D is the tube diameter, $D_{\min}$ is the stenosis throat diameter, and L is its length. Here, $D/D_{\min} = L/D = 2$.

In order to quantify the axisymmetric inflow $u(r,t)$ of temporal period T we use the sectional average

$$\bar{u}(t) = (8/D^2)\int_0^{D/2} u(r,t)\, r\, \mathrm{d}r,$$

and temporal average

$$\bar{u}_m = \frac{1}{T}\int_0^T \bar{u}(t)\, \mathrm{d}t.$$

For given $\bar{u}(t)$ we can define at least three independent dimensionless groups: the reduced velocity U_{red}, the peak-to-mean flow ratio, and the Reynolds number Re, respectively given by

$$U_{red} = \bar{u}_m T/D, \qquad U_{pm} = \max_{0\leqslant t\leqslant T} \bar{u}(t)/\bar{u}_m = \bar{u}_{\mathrm{peak}}/\bar{u}_m, \qquad Re = \bar{u}_m D/\nu,$$

where ν is the kinematic viscosity of the fluid. An additional non-independent dimensionless parameter, the Womersley number $\alpha = (\pi Re/2U_{red})^{1/2} = (2\pi/T\nu)^{1/2}D/2$, is also commonly used in this applications area, following the pioneering analytical work on pulsatile flows in straight tubes by Womersley (1955). We prefer to use the reduced velocity so that the effect of viscosity is parameterised only by Reynolds number, and because the reduced velocity has a simple physical interpretation as the dimensionless distance travelled by the bulk flow in one pulse period. The reduced velocity can also be thought of as a dimensionless pulse period. The single-harmonic sectional-average flow temporal waveform considered in the present work is

$$\bar{u}(t) = \bar{u}_m\left[1 + a_1 \sin\left(2\pi t/T\right)\right], \tag{1.1}$$

as illustrated in figure 1 (*b*). This is the same as the single-harmonic waveform chosen in

Sherwin & Blackburn (2005) and with $a_1 = 0.75$. For this value the waveform has a peak-to-mean ratio of $U_{pm} = 1.75$.† In § 6, we also examine convective shear layer instability with the much smaller amplitude $a_1 = 0.001$ which can be considered as a perturbation to steady inlet flow.

Inlet flows are computed from Womersley's solution for fully developed periodic pulsatile laminar flow in a circular tube, which is the sum of Fourier–Bessel components at each temporal harmonic n defined by

$$u_n(r,t) = \mathrm{Re}\left[\frac{A_n \mathrm{i} T}{\rho 2\pi n}\left(\frac{J_0(\mathrm{i}^{3/2}\alpha\, 2r/D)}{J_0(\mathrm{i}^{3/2}\alpha)} - 1\right)\exp 2\pi\,\mathrm{i}nt/T\right], \tag{1.2}$$

where $\mathrm{i} = (-1)^{1/2}$, J_0 is the complex Bessel function of zeroth order, ρ is the fluid density, and α is the aforementioned Womersley number. The parameter A_n is a complex number representing the driving pressure gradient $\partial_z p = A_n \exp 2\pi\,\mathrm{i}nt/T$ which can be determined from a specified sectional-average velocity $\bar{u}(t)$ at a given harmonic. In the present study, we have restricted consideration to $n = \{0, 1\}$; when $n = 0$, (1.2) reduces to the standard parabolic Hagen–Poiseuille profile for steady flow.

As is commonly justified in many works on blood flows in the major arteries, Newtonian rheology has been assumed. While the effect of artery wall compliance is potentially important, it has been ignored in the present work on the assumption that the major role of wall compliance — a distributed property — will be to influence the shape of the waveform reaching a given site, rather than to significantly affect local flow dynamics. For discussion of these assumptions and reviews on blood flow in arteries, the reader is referred to Ku (1997), Wootton & Ku (1999), Berger & Jou (2000) and Taylor & Draney (2004).

1.2. *Outline of paper*

In § 2 the numerical methods employed are described in brief, having been described in greater detail in Sherwin & Blackburn (2005). The effect of variation in reduced velocity (pulse period) on base flows at fixed $Re = 400$ is examined in § 3. In § 4 we use Floquet stability analysis and three-dimensional DNS to study the effect of U_{red} on the period-doubling mode: this is a superset of the three single-harmonic results presented in our earlier paper. We also introduce phase-averaged statistics to help quantify the corresponding effect of U_{red} on time-asymptotic turbulent flows following transition; the locations of turbulent breakdowns may evolve to locations considerably upstream of the location of the peak Floquet mode amplitude. In § 5 we show that at lower reduced velocities (shorter pulse periods) than for the period-doubling mode, the primary instability manifests as azimuthal waves, evocative of the Widnall modes observed for isolated vortex rings (Widnall, Bliss & Tsai 1974), and again we also study the flow following transition using three-dimensional DNS. At still shorter periods, the shear layers of steady stenotic flow are found to be susceptible to a convective instability, which we examine by adding a harmonic perturbation to the inflow in axisymmetric DNS; this aspect is dealt with in § 6. The whole study is summarised and discussed in §§ 7 and 8.

2. Numerical methods

The study addresses the linear Floquet stability and direct numerical simulation of the incompressible Navier–Stokes equations, which are treated in cylindrical coordi-

† Naturally occuring arterial flows have a broader frequency content and often also have a higher peak-to-mean ratio, although lower values are also observed.

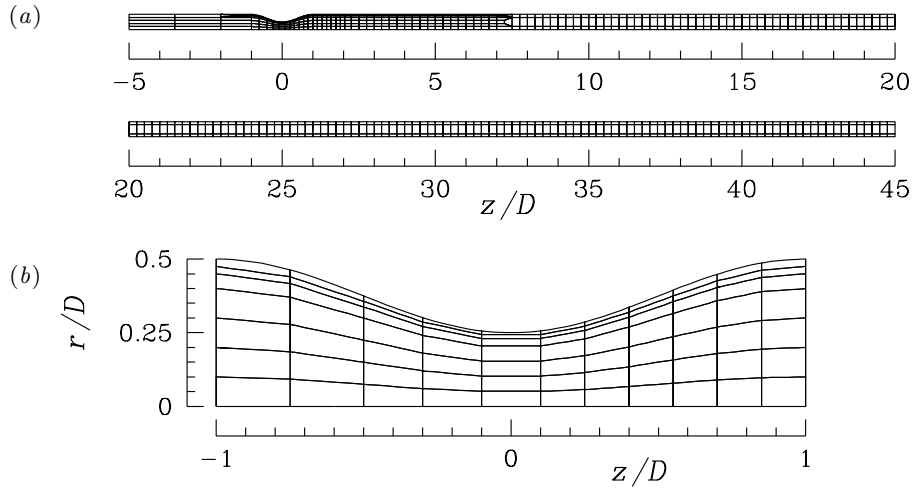

FIGURE 2. Computational mesh in the meridional semiplane. (*a*) Layout of the 743 spectral elements. (*b*) Close up of the stenosis.

nates (z, r, θ). The spatial discretisation couples spectral elements having nodal Gauss–Lobatto–Legendre (GLL) basis functions in the meridional semiplane with Fourier basis functions in azimuth. Temporal integration is performed using a mixed implicit-explicit velocity correction scheme of second order. For details of the numerical methods and their prior application to this problem, consult Blackburn (2002); Blackburn & Sherwin (2004); Sherwin & Blackburn (2005). Regarding stability analysis of the non-axisymmetric modes, it should be noted that all the bifurcations in this work occur through pitchforks of revolution, where the non-axisymmetric mode shapes can be arbitrarily rotated about the cylindrical axis.

The spectral element macro mesh employed both in the present study and in the single-harmonic component of Sherwin & Blackburn (2005) is illustrated in figure 2. There are 743 spectral elements, concentrated around the stenosis throat and where the separated shear layers are most fine. The comparatively long outflow was found necessary to accommodate and resolve the Floquet modes, which can reach their greatest amplitude some distance downstream of the stenosis. In the previous study, a GLL basis function order $N_p = 7$ was found adequate to resolve Floquet multipliers to approximately four-figure accuracy, and has been retained through the present work. The mesh has approximately 38 000 independent degrees of freedom for each azimthal plane.

3. Axisymmetric base flows

The primary visual feature of pulsatile stenotic flow is vortex rings that form downstream of the stenosis from rollup of the shear layer that separates in the throat, just past the location of minimum cross-section. When only a single harmonic is present, a single ring forms with each pulse period. Figure 3 shows the effect of reduced velocity (dimensionless period) on the vorticity contours of the axisymmetric flows. In this plot all simulations are at a Reynolds number of 400 and at phase point $t = nT$. As may be expected, the effect of increasing U_{red} is to increase the axial spacing of successive vortex rings. This also has the consequence of producing a very elongated shear layer as U_{red} increases. For the lower reduced velocities (figure 3 *a*, *b*) there is also some indication of secondary structures appearing near the first fully separated vortex ring.

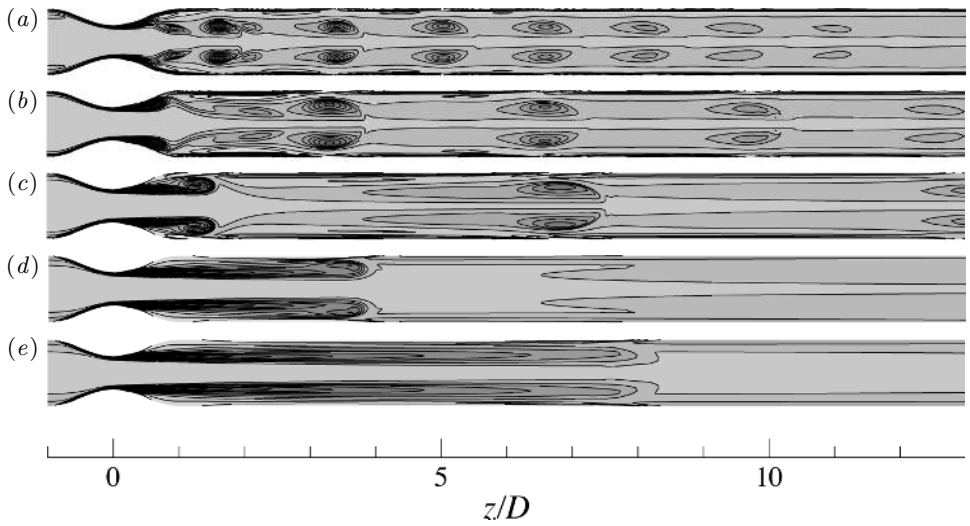

FIGURE 3. The effect of pulse period on base flow vorticity on a section through the tube centreline at $Re = 400$. Vorticity contours at (a), $U_{red} = 0.5$, $\alpha = 33.45$; (b), $U_{red} = 1$, $\alpha = 25.07$; (c), $U_{red} = 2$, $\alpha = 17.72$; (d), $U_{red} = 5$, $\alpha = 11.21$; (e), $U_{red} = 10$, $\alpha = 7.93$.

Gharib, Rambod & Shariff (1998) and Rosenfeld, Rambod & Gharib (1998) have proposed a universal dimensionless time scale, called the formation number, related to the formation of unconstrained vortex rings from an impulsive jet discharging into open space. The formation number is associated with a vortex ring acquiring maximal circulation and pinching off from its trailing jet, and is given by $L_{\max}/D_{\rm jet} \approx 4$, where $L_{\max}$ is the integrated length of jet discharge (i.e. jet discharge velocity integrated over time) up until the front rolls up and pinches off from the jet. The implication of this result is that at a fixed Reynolds number, if the formation time of the vortex ring is sufficiently long (i.e. above the 'formation number' of 4) the vortex ring formed in each pulsatile cycle will have a similar circulation, independent of the reduced velocity. In the absence of other influences the circulation of vortex ring dictates its self-induced velocity. Therefore if we ignore the role of the pipe walls, the distance a vortex ring will propagate during each pulsatile cycle will be dependent on the induced velocity and the pulsatile time period. If for the present situation we assume that the vortex ring is generated during half the pulsatile period, then, since the jet is generated at the stenosis throat where $D_{\rm jet} = D/2$ and the average jet velocity is $4\bar{u}_m$, the maximum formation time in our problem is of order $(T/2) \cdot 4\bar{u}_m/(D/2) = 4U_{red}$. Therefore if a universal formation number exists for constrained vortex rings and is similar to the value obtained by Gharib *et al.* (1998) for unconstrained flows, then for $U_{red} \geq 1$ we would expect a vortex separation which scales linearly with the dimensionless period (or reduced velocity).

To investigate this point we show in figure 4 the axial distance Δz between successive identifiable vortex rings (whose locations are taken as those of the local maxima of vorticity), normalised by $\bar{u}_m T$. We note that since in the downstream limit the vortex ring has almost zero strength and advects with the mean flow the ring spacing must tend to the distance the mean flow travels in one pulse period and so $\Delta z/\bar{u}_m T \to 1$. This trend is clearly evident in figure 4 where we see that at all reduced velocities as the vortex rings become weaker under the action of diffusion there is an asymptotic trend for $\Delta z/\bar{u}_m T$ to tend to unity.

On the other hand if we consider the first ring spacing we observe that for nearly all the

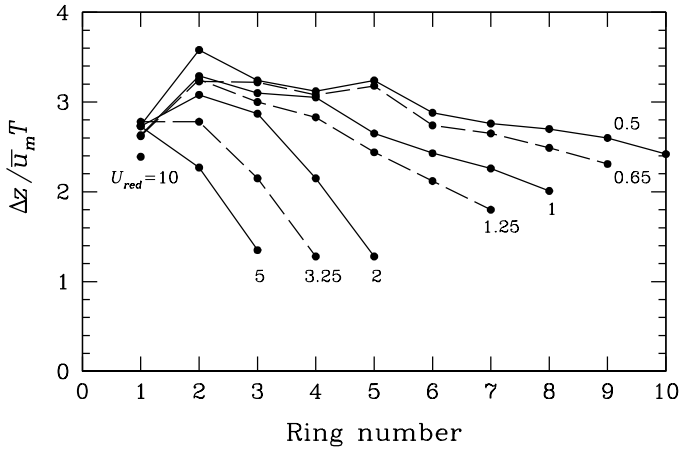

FIGURE 4. Dimensionless axial spacing of base flow vortex rings at $t = nT$, at various values of U_{red} for $Re = 400$.

reduced velocities there is a similar normalised spacing of $\Delta z/\bar{u}_m T \approx 2.8$ which supports the idea of a fixed formation number on the constrained vortex ring. At the higher reduced velocities $U_{red} \geq 3.25$ the subsequent ring spacing becomes smaller and tends to the asymptotic value of one. However for the lower reduced velocities $U_{red} < 3.25$ the few ring spacings after the initial ejection tend to have an increased spacing with a maximum value of approximately three. This increase in ring spacing is potentially related to the constrained nature of the flow environment and its associated image system. However the fact that we only observe this increased spacing at lower reduced velocities would tend to suggest that the closer proximity of the downstream vortex rings may also be a factor in determining the increased spacing.

4. Period doubling instability mode

Axisymmetric time-periodic base flows are the state about which we linearise prior to conducting Floquet analysis for three-dimensional instabilties. At any reduced velocity, base flows are pre-computed for a range of Reynolds number, and the dominant Floquet multiplier μ and its associated eigenfunction (at a specific phase point t/T) is established at each Reynolds number. By interpolating to $|\mu| = 1$ the marginal stability Reynolds number is established, as shown in figure 14 of Sherwin & Blackburn (2005). All the pulsatile flow instability modes discovered in that study had $\mu_c = -1$, which corresponds to a period-doubling bifurcation. The instability can be physically associated with a tilting of the vortex rings, and the period-doubling mechanism was shown to be that the downwash induced by this tilting in the wake of one ring drives an opposite tilt on the succeeding ring. Because the mechanism of this instability mode was described in some detail in Sherwin & Blackburn (2005), our treatment of this aspect here will be somewhat abbreviated, and concentrate more heavily on the effects of variation of pulse period.

4.1. *Linear stability*

The tilting mechanism necessarily arises in the first azimuthal Fourier mode, wavenumber $k = 1$. In figure 5 we show an example wavenumber spectrum of Floquet multiplier magnitudes computed at $U_{red} = 3.25$, $Re = 400$, which shows all the other modes to be comparatively stable, and the subdominant mode to occur at $k = 4$.

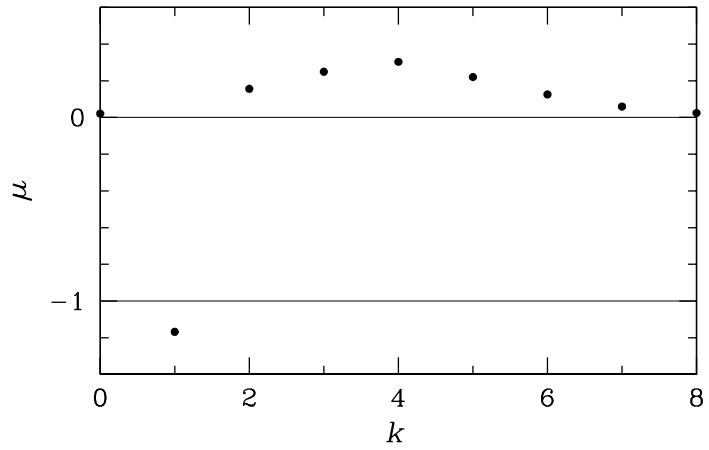

FIGURE 5. Azimuthal wavenumber spectrum of Floquet multipliers at $U_{red} = 3.25$, $Re = 400$. The negative multiplier of the unstable mode indicates a period-doubling instability.

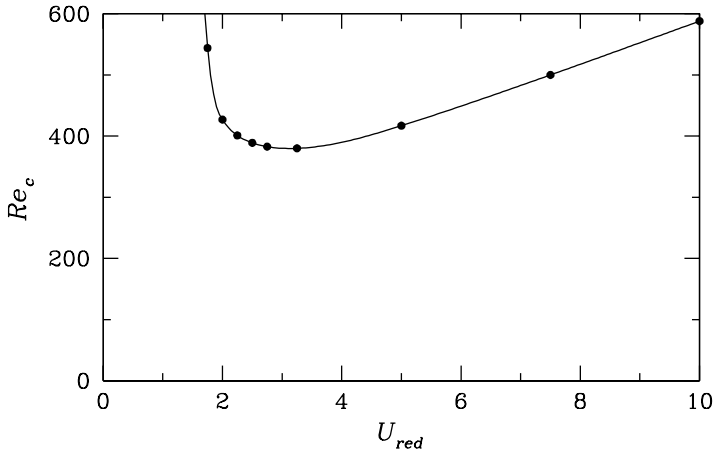

FIGURE 6. Critical curve of the $k = 1$ period-doubling instability mode as a function of reduced velocity.

Through the process of interpolation at each reduced velocity, we have established the curve of marginal stability of the period-doubling mode as a function of U_{red}, shown in figure 6. An 'optimal' reduced velocity (minimum Re_c) occurs near $U_{red} = 3.25$, where $Re_c = 380$. At $U_{red} < 2$, Re_c for this mode grows rapidly to high values, while it appears that in the high U_{red} limit, Re_c grows approximately linearly with U_{red}.

Figure 7 provides a number of contour plot pairs of instantaneous energy per unit mass $q = \boldsymbol{u}^2/2$ in the base flow and also the logarithm of q for the corresponding period-doubling mode, both illustrated at the phase point $t = nT$ for various U_{red} and at Re close to Re_c. The pair (e, f) at $U_{red} = 3.25, Re = 400$ corresponds to the optimum wavenumber in figure 6. The pulsatility of the base flows is readily observed: each local maximum of q here corresponds to a vortex ring. It can be seen that as the optimum reduced velocity, $U_{red} = 3.25$, is approached from below the peak energy in the Floquet modes migrates upstream towards the stenosis and is associated with successive vortex rings located closer to the stenosis. However, in all these cases as a downstream traverse is

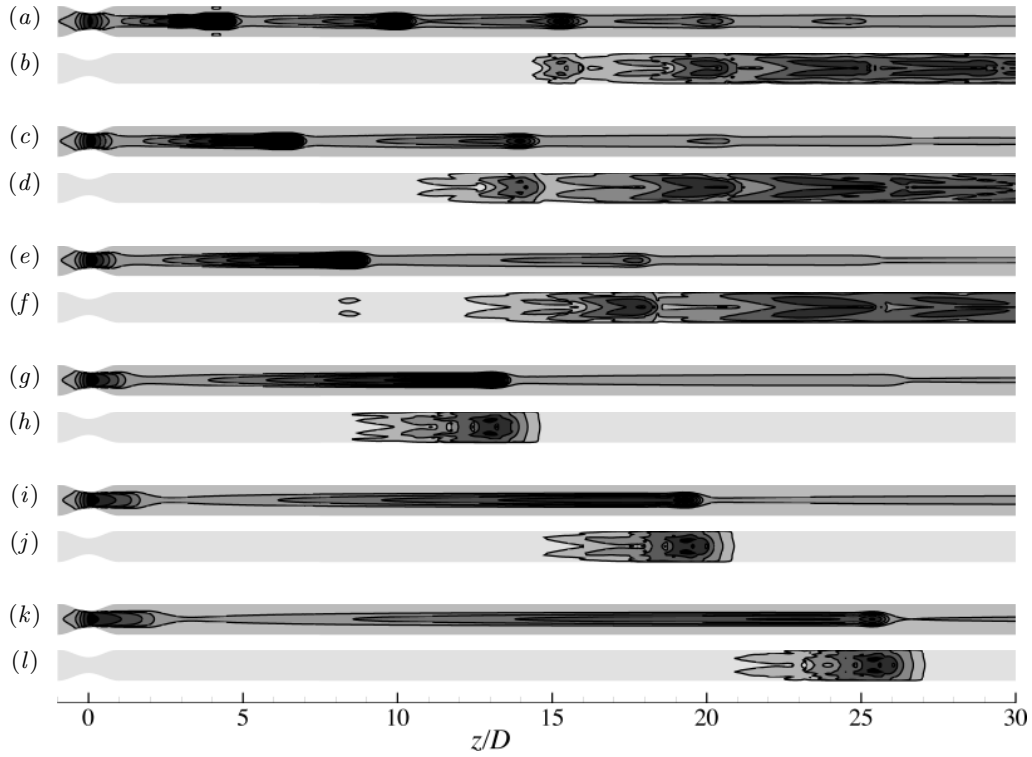

FIGURE 7. Contour plot pairs showing instantaneous energy q in the base flow (top of pair) and logarithm of energy in the period-doubling Floquet instability mode (bottom of pair) on a plane containing the tube centreline for: (a, b) $U_{red} = 1.75$, $Re = 545$; (c, d) $U_{red} = 2.5$, $Re = 389$; (e, f) $U_{red} = 3.25$, $Re = 370$; (g, h) $U_{red} = 5$, $Re = 415$; (i, j) $U_{red} = 7.5$, $Re = 500$; (k, l) $U_{red} = 10$, $Re = 590$. Results are all close to marginal stability and shown at phase point $t = nT$. Eigenmodes were pre-normalised to the same energy level and have energy contours are drawn at decade-and-a-half intervals. Note that the visualised region is $15D$ shorter than the computational domain.

made from one base flow vortex to the next the Floquet modal energy grows and then dies away. This may well be indicative of a competition between modal energy growing with distance downstream while the energy of the base flow pulses, that feed the instability, is dying away.

At $U_{red} = 3.25$, modal energy contours can just be observed starting to appear on the first base flow pulse downstream of the stenosis, at $z/D \approx 8$. At higher reduced velocities we observe that the Floquet mode's energy is associated with just the first vortex downstream of the stenosis; this is confirmed by the pair (e, f) where there is no observable modal energy on the second visible base flow pulse downstream of the stenosis. We may therefore attribute the asymptotic high-U_{red} behaviour seen on the critical curve in figure 6 (where Re_c grows linearly with U_{red}) to this change in structure of the spatial Floquet energy wih respect to the base flow vortex ring location.

4.2. *Nonlinear asymptotic states*

In DNS studies we initiate simulations with a three-dimensional projection of an axi-symmetric base flow at a slightly unstable Reynolds number superimposed with a small amount of the dominant Floquet mode at a relatively small energy level. The simulation is then integrated forward in time until an asymptotic, statistically stationary state is

FIGURE 8. Two visualisations of the asymptotic turbulent state for $U_{red} = 2.5$, $Re = 400$, at a time interval $\Delta t = T$. Instantaneous isosurfaces of velocity gradient tensor discriminant $\mathcal{D}$, and equal magnitudes of positive and negative streamwise vorticity component. In each view, the first well-organised set of structures downstream of the throat represents a vortex ring that has commenced to tilt and distort; the second less-organised set results from the breakdown of the two preceding vortex rings. Note that the flow at times (a) and (b) forms almost exact mirror images, consistent with the underlying period-doubling instability.

reached. As explained in Sherwin & Blackburn (2005) this evolution may take the order of hundreds of pulse periods to achieve. The typical behaviour is for the instability to gain an initial saturation relatively quickly, with weakly nonlinear behaviour that could be modelled using a low-order normal form. During this phase the maximum three-dimensional energy arises in approximately the same axial location as for the Floquet mode. Subsequently however, there is a long second saturation to the asymptotic state, in which the peak three-dimensional energy evolves slowly upstream towards the stenosis. As this happens the amount of three-dimensional energy in the flow also increases, associated with the flow making a localised transition to turbulence, but also with the fact that the energy of the vortex rings that feed the instability is greater upstream. In the asymptotic state the transition typically appears on the vortex ring blown out of the stenosis, even though the peak energy of the Floquet mode may have arisen far downstream.

Figure 8 illustrates the asymptotic state for $U_{red} = 2.5$, $Re = 400$ at phases $t = nT$ and $t = (n + 1)T$, i.e. one pulse period apart.† Three instantaneous isosurfaces are used. An isosurface drawn on a positive value of the discriminant $\mathcal{D}$ of the velocity gradient tensor in order to pick out the pulse-driven vortex rings. As outlined in Blackburn, Mansour & Cantwell (1996), such structures will contain motions with a local vortical motion and serve as markers for isolated vortices. The other two isosurfaces are drawn on equal-magnitude postive and negative values of axial vorticity component; these emphasise the departure of the flow from axisymmetry.

In figure 8 (a) there is an isolated, completely axisymmetric isosurface of $\mathcal{D}$ located in the stenosis throat, while approximately $2.5D$ downstream isolated vortex ring may be seen; tilting streamwise at the top of the tube, and is accompanied near the centerline by two isosurfaces of streamwise vorticity component as it begins to distort three-dimensionally. Approximately one further diameter downstream there is a tangle of interlocked isosurfaces that marks a weakly turbulent breakdown of two previous vortex rings. Note also that the dominant tilt at the upstream end of this tangle seems to be the reverse of that for the approaching vortex ring. The breakdown dissipates further downstream however, and by approximately $8D$ downstream relaminarisation is well underway. Eventually the laminar pulsatile flow profile of the inlet flow is regained, although we have not studied the approach to this state in detail.

Now comparing figure 8 (b) to figure 8 (a) the period-doubling nature of the instability is readily seen, since the second image is nearly an exact reflection about a horizontal plane of the first. This is true even at the upstream end of the apparently turbulent

† See Sherwin & Blackburn (2005) for details of the progression to this asymptotic state.

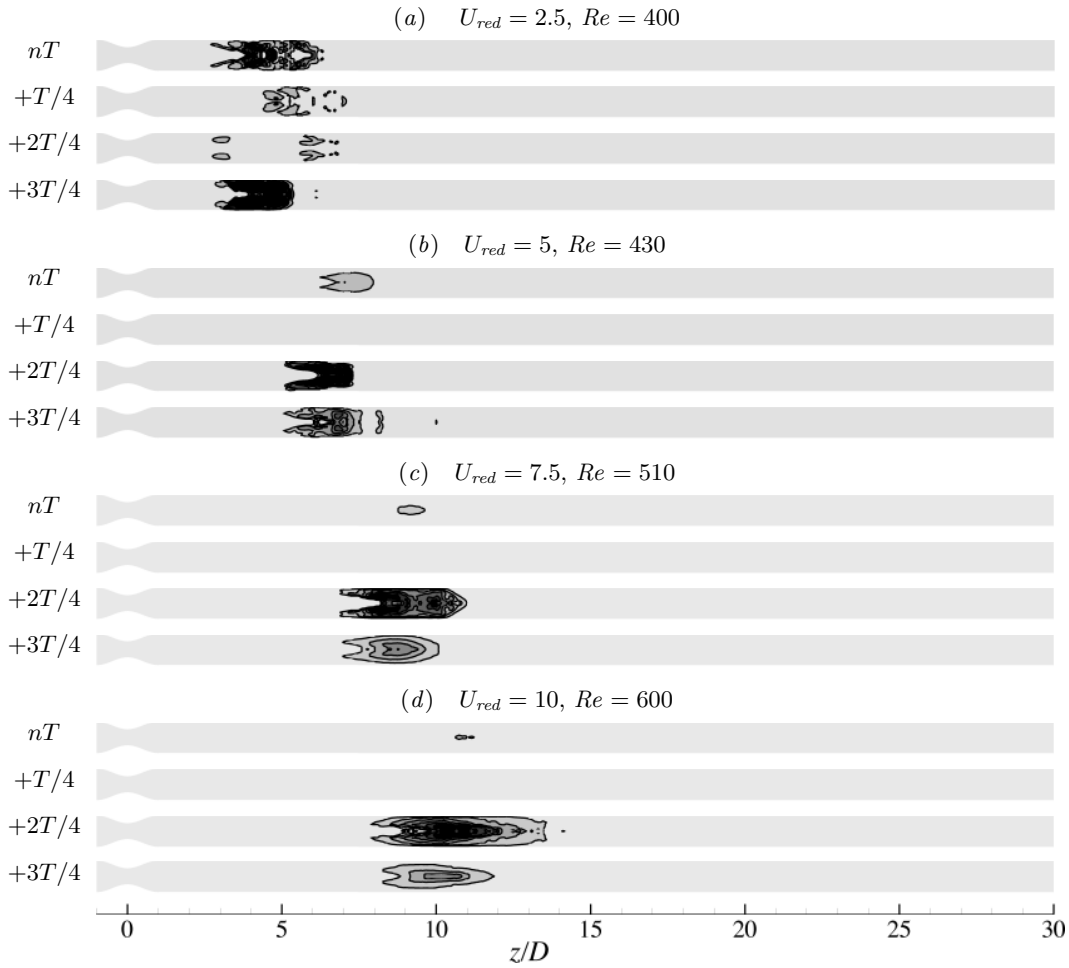

FIGURE 9. Contours of phase-averaged turbulent energy on a slice through the pipe centreline at four temporal phases for the asymptotic states at (*a*) $U_{red} = 2.5,\ Re = 400$; (*b*) $U_{red} = 5,\ Re = 430$; (*c*) $U_{red} = 7.5,\ Re = 510$; (*d*) $U_{red} = 10,\ Re = 600$.

burst, and the effect is still quite strong near its downstream limit. This feature persists even when the solution is perturbed through the addition of low-energy random noise.

All the period-doubling instabilities that we have investigated via DNS have shown broadly similar behaviour, in that there is a slow migration of the breakdown point upstream to an asymptotic location, and the breakdown is followed by relaminarisation downstream, while the period-doubling nature of the instability is retained. As was remarked in § 6.4.4 of Sherwin & Blackburn (2005), the overall description of behaviour seen here is in many ways similar to the experimental flow visualisation observations made by Ojha *et al.* (1989) at $Re = 575$, $U_{pm} = 1.6$ and $U_{red} = 16.1$ in a tube with a sharp-edged 2:1 diametral contraction. They did not report period-doubling behaviour, but were perhaps not aware of this possibility.

Now we turn to examination of the phase-averaged flows in the asymptotic states for cases ($U_{red} = 2.5,\ Re = 400$), ($U_{red} = 5,\ Re = 430$), ($U_{red} = 7.5,\ Re = 510$) and ($U_{red} = 10,\ Re = 600$). By inspection of figure 6 the Reynolds numbers will be seen to be just slightly greater than the critical values at each reduced velocity. The number of

azimuthal Fourier modes (half the number of planes of data) was set to 16, 24, 24 and 32 respectively, producing approximately 1.2, 1.8, 1.8 and 2.4 million grid points for the four cases, in recognition of the increasing Reynolds numbers. It has been verified that the spread of energies from the first to the last non-axisymmetric mode in each case spans at least three decades, which is thought to be sufficient given the resolution in the meridional semiplane. The quantity examined is the turbulent energy $q' = \boldsymbol{u}'^2/2$ after the mean and periodic flows have been removed (Reynolds & Hussain 1972). Considering that only a single contribution to a phase average can be accumulated in each pulse period, we have restricted these calculations to averages over 50 periods; as this is an even number, any alternation associated directly with period-doubling is averaged out. For each flow we have computed eight phase averages at $t_i = (n + i/8)T$, then their azimuthal averages and finally extracted contours of q'. Outcomes are presented as two-dimensional contour plots on a plane containing the tube centreline; in order to save space we have presented only four of the eight phases collected. Note that contour levels are identical in each case.

Figure 9 (*a*) shows the set of contours for phase-averaged turbulent energy computed in this manner for ($U_{red} = 2.5$, $Re = 400$), i.e. corresponding to the state illustrated in figure 8. There is evidently quite an amount of spatial structure to the random fluctations, in agreement with the qualitative remarks made above in relation to figure 8. We see that the turbulent energy is effectively contained within an approximately $4D$-long region commencing at $z/D \approx 2.5$. Note the contrast with the linear Floquet mode seen for the same reduced velocity in figure 7 (*d*), where the greatest modal energy arises near $z/D = 20$.

Figures 9 (*b*–*d*) show the phase-average outcomes in the asymptotic states at ($U_{red} = 5$, $Re = 430$), ($U_{red} = 7.5$, $Re = 510$) and ($U_{red} = 10$, $Re = 600$), respectively. Very much the same pattern of behaviour as seen in figure 9 (*a*) is observed, but the location of the turbulent burst moves downstream as U_{red}, or equivalently dimensionless pulse period, increases. The axial spread of the energy across a pulse period remains approximately $4D$, and the amount of energy decreases as the breakdown locations move downstream with increasing U_{red}.

5. Wavy instability modes

5.1. *Linear instability*

In figure 6 it is observed that Re_c for the period-doubling mode increases rapidly as U_{red} decreases to values below two. Also, in figure 5, a subdominant mode is observed at wavenumber $k = 4$. It transpires that for a range of reduced velocities $U_{red} < 2$, the set of modes $k > 1$ that are stable at higher reduced velocities grow to dominate, as exemplified in figure 10 which shows the spectrum of Floquet multipliers at $U_{red} = 0.875$, $Re = 350$, where both $k = 3$ and $k = 4$ host unstable modes, and the one at $k = 3$ dominates. Note that now the dominant multipliers are real and positive, and hence the modes are synchronous with the base flow.

The marginal-Re stability curves for the $k = 3$ and $k = 4$ modes compete for dominance, as shown in figure 11 where it is seen that for $U_{red} \gtrapprox 1.5$, the $k = 4$ mode is the least stable, while at lower reduced velocities the $k = 3$ mode becomes the slightly less stable of the pair. Like the period-doubling mode, the wavy modes have an 'optimal' reduced velocity (now near $U_{red} = 0.875$); at lower values the marginal stability Reynolds numbers increase rapidly with falling U_{red}, while in the high-U_{red} limit, there is again an approximately linear variation of Re_c with U_{red} for both modes.

Figure 12 uses isosurface visualisation to illustrate the structure of these wavy modes

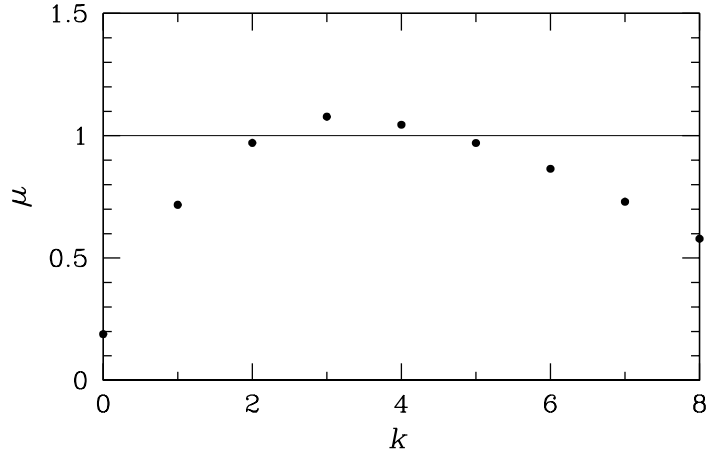

FIGURE 10. Azimuthal wavenumber spectrum of Floquet multipliers at $U_{red} = 0.875$, $Re = 350$. Wavy modes with both $k = 3$ and $k = 4$ are unstable.

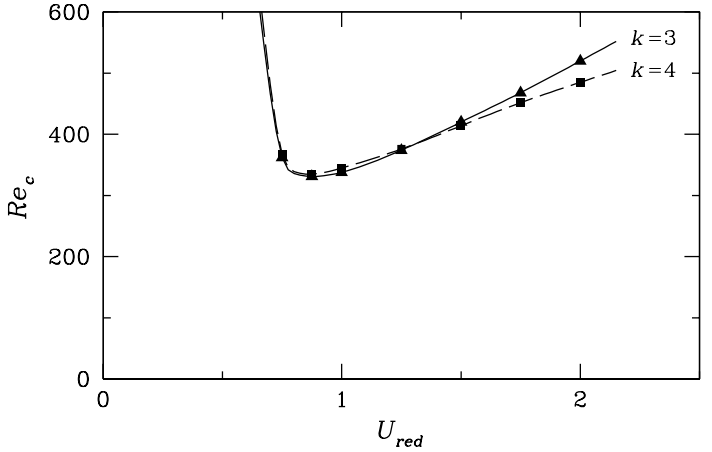

FIGURE 11. Critical curves for the wavenumber $k = 3$ and $k = 4$ wavy modes.

at $U_{red} = 0.875$, $Re = 325$, slightly below the marginal stability value of $Re_c = 335$ for the $k = 3$ mode. We have used an isosurface of a positive value of the discriminant $\mathcal{D}$ of the velocity gradient tensor for the base flow to show the locations of vortex rings, while the linear instability modes are shown using equal-magnitude positive/negative values of streamwise vorticity component. Note that in this figure there is by definition no distortion of the base flow vortices, which have been shown to reveal the spatial relationship between the instability modes and the base flow.

In figure 12 (*a*), the $k = 3$ instability mode can be seen to begin growing in an isolated manner on the second vortex downstream of the stenosis. Therefore this is a type of wavy vortex ring instability (e.g. Widnall *et al.* 1974). It seems however that as the modal energy grows downstream there is significant axial linkage between the three-dimensional instability growing on sequentially created rings. If anything, this phenomenon seems stronger for the $k = 4$ instability seen in figure 12 (*b*). Thus it seems unlikely that these modes could be analysed by examining the stability of an isolated vortex ring.†

† This expectation is supported by our (otherwise unreported) attempts to carry out

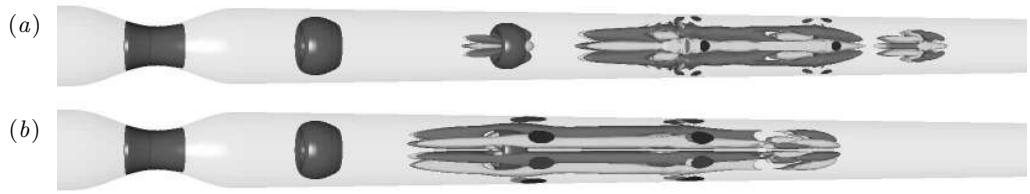

FIGURE 12. Isosurfaces illustrating the (a) wavenumber $k = 3$ and (b) wavenumber $k = 4$ wavy instability modes at $U_{red} = 0.875$, $Re = 325$, at phase point $t = nT$. Vortex rings of the base flow are visualised on a positive value of the velocity gradient tensor discriminant $\mathcal{D}$, while the wavy mode shapes (with predominantly axial alignment) are visualised using equal-magnitude but oppositely signed values of axial vorticity component.

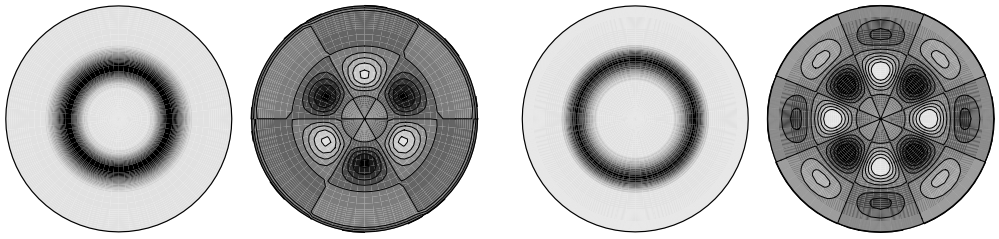

FIGURE 13. Structure of the wavy modes in cross-section. for $U_{red} = 0.875$, $Re = 325$, phase point $t = nT$. (a) Contours of velocity gradient tensor discriminant $\mathcal{D}$ (black, positive) for the base flow at $z/D = 7.75$ and (b) contours of $k = 3$ Floquet mode radial velocity component at the same axial station. (c, d) Equivalent contours at axial station $z/D = 4.95$, $k = 4$ Floquet mode.

More detail of the cross-sectional structure of the base flow and instability modes can be seen in figure 13, again for $U_{red} = 0.875$, $Re = 325$, $t = nT$. Figure 13 (a, b) show respectively a contour of velocity gradient discriminant $\mathcal{D}$ in the base flow and a contour of radial velocity component of the $k = 3$ Floquet mode, at station $z/D = 7.75$, while figure 13 (c, d) show corresponding contours for the $k = 4$ mode, at station $z/D = 4.95$. While contours of $\mathcal{D}$ for the base flow indicate vortex structures apparently confined to $r/D \lessapprox 0.3$, the spread of positive azimuthal vorticity on the same sections is rather more diffuse, reaching from $r/D = 0$ to $r/D \approx 0.45$ with a maximum near $r/D = 0.23$. The radial structure of each Floquet mode contains two nodes, which conforms to the predictions of Widnall *et al.* (1974) for short-wavelength instabilities on isolated vortex rings, even though the current rings cannot be considered slender (of small core/radius ratio) as was the case in their analysis.

Figure 14 shows pairs of plots of contours of energy in the base flows and the logarithm of energy in the $k = 3$ modes for a progressive increase in reduced velocity. The modal energy contours in each case show that for these modes, energy is always spread in an apparently connected manner across a number of base flow pulses/vortices. The optimum U_{red} (near $U_{red} = 0.875$, figure 14 e, f) is, as was the case for the period-doubling mode, again associated with modal energy finding its furthest-upstream location.

5.2. *Nonlinear evolution*

Under nonlinear evolution from a base flow seeded with the instability mode, a similar sequence of events is found as was the case for the period-doubling mode. Starting with

quasi-steady stability analysis of a single vortex ring clipped from the base flow and isolated from its neighbours, which have failed to reproduce dominance of the $k = 3$ or $k = 4$ modes.

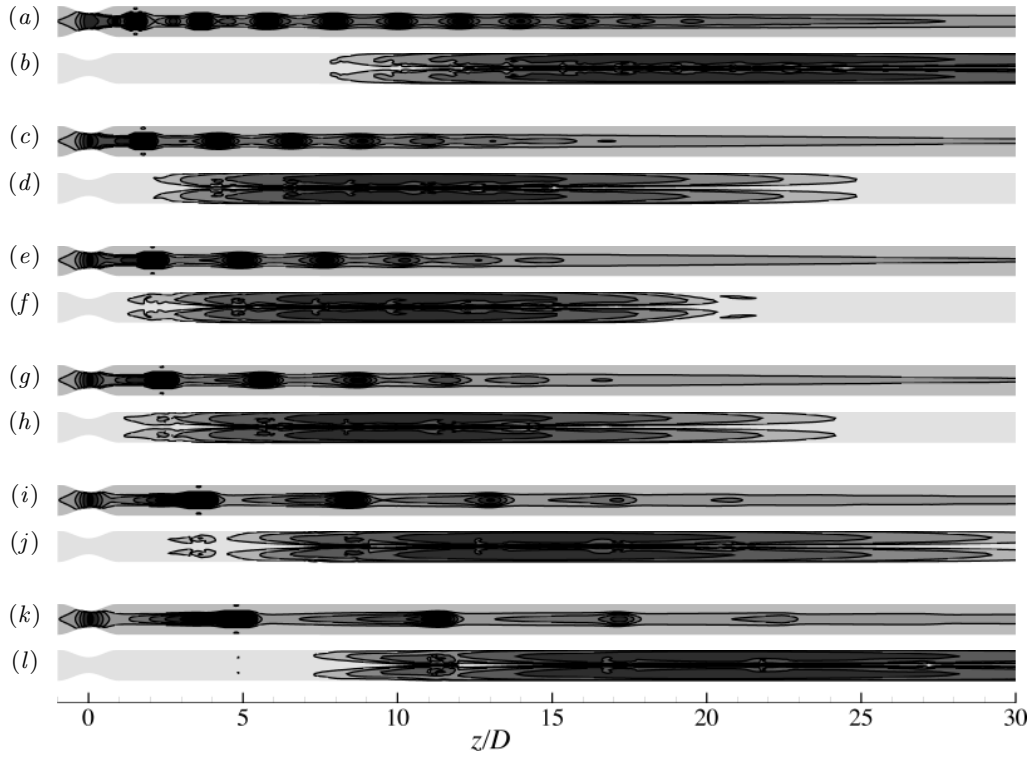

FIGURE 14. Contour plot pairs showing instantaneous energy in the base flow and logarithm of energy in wavy-ring Floquet instability mode at azimuthal wavenumber $k = 3$ for: (a, b) $U_{red} = 0.65$, $Re = 600$; (c, d) $U_{red} = 0.75$, $Re = 350$; (e, f) $U_{red} = 0.875$, $Re = 325$; (g, h) $U_{red} = 1$, $Re = 339$; (i, j) $U_{red} = 1.5$, $Re = 425$; (k, l) $U_{red} = 2$, $Re = 500$. Results are all close to marginal stability and shown at phase point $t = nT$. Eigenmodes were pre-normalised to the same energy level and have energy contours are drawn at decade-and-a-half intervals.

initial exponential growth, there is a first weakly nonlinear saturation with the peak energy occuring in an axial location similar to that for the Floquet mode, and this is followed by a second slow saturation to the asymptotic state. Again the asymptotic state possesses a localised turbulent breakdown, and subsequently the slow second saturation is associated with an upstream migration to a limit of the site of this breakdown.

Figure 15 illustrates the three-dimensional transitional flow at $U_{red} = 1$, $Re = 350$, at (a), the end of the first weakly nonlinear saturation and (b), in the asymptotic state. As in figure 8, the flows are visualised using the discriminant of the velocity gradient tensor (to show the vortex rings) and positive/negative streamwise vorticity (to emphasise three-dimensional behaviour). In figure 15 (b) it can be seen that in the asymptotic state, three-dimensional instability reaches upstream to begin vortex ring distortion almost immediately following detachment, and this is linked directly to the breakdown of the previously created vortex ring.

Figure 16 shows contours of phase-average (and also azimuthal-average) turbulent energy q' for the asymptotic state at $U_{red} = 1$, $Re = 350$. Contour levels are the same as for figure 9. The energy is confined very close to the stenosis, z/D in the range 1–5.

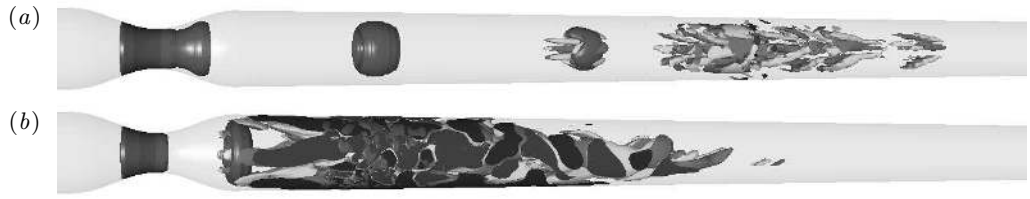

FIGURE 15. Two visualisations of the turbulent state for $U_{red} = 1$, $Re = 350$; instantaneous iso-surfaces of $\mathcal{D}$ representing vortex ring structures, and equal magnitudes of positive and negative streamwise vorticity component to emphasise three-dimensionality and turbulence. At time (a), the flow has completed an initial nonlinear saturation, while a number of pulse cycles later in (b), the flow has reached an asymptotic state and turbulent breakdown occurs just a few tube diameters downstream of the throat.

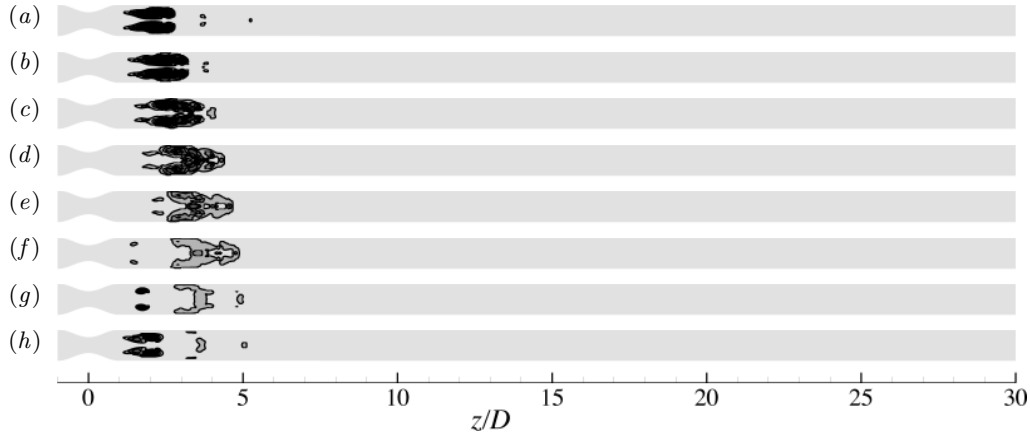

FIGURE 16. Contours of phase-averaged turbulent energy q' on a slice through the pipe centreline for the asymptotic state at $U_{red} = 1$, $Re = 350$ for phases: (a) $t = nT$; (b) $t = (n + 1/8)T$; (c) $t = (n + 2/8)T$; (d) $t = (n + 3/8)T$; (e) $t = (n + 4/8)T$; (f) $t = (n + 5/8)T$; (g) $t = (n + 6/8)T$; (h) $t = (n + 7/8)T$.

6. Convective shear layer instability of steady flows

As pulse periods are reduced still further below $U_{red} \sim 0.6$, no other Floquet instability modes have been identified. However, in Sherwin & Blackburn (2005), it was found that the extended shear layer for a two-harmonic pulsatile base flow was susceptible to a high-frequency convective instability, and also shear-layer oscillations were observed in DNS of the steady-inflow case at $Re = 750$ (see figure 9 of that paper). Using those observations as a starting point we have conducted a more systematic study of convective shear layer instability in our stenotic system driven by a steady base flow plus a high frequency (low reduced velocity) perturbation. The methodology is similar to that described in § 6.4.3 of Sherwin & Blackburn (2005), where axisymmetric DNS was employed. Since by definition a convective instability will eventually wash out of the domain in the absence of perturbation, we drive it by adding a small amplitude harmonic streamwise perturbation to the mean inflow boundary condition, as described by (1.1) with $a_1 = 0.001$. It is found that over a comparatively narrow frequency/reduced velocity band, this type of perturbation excites oscillations in the separated shear layer downstream of the stenosis throat and may induce shear-layer rollup.

Our measure of the response is chosen as the fluctutating radial velocity component at $(z/D = 2.5,\ r/D = 0.25)$ i.e. one-and-a-half diameters downstream of the end of

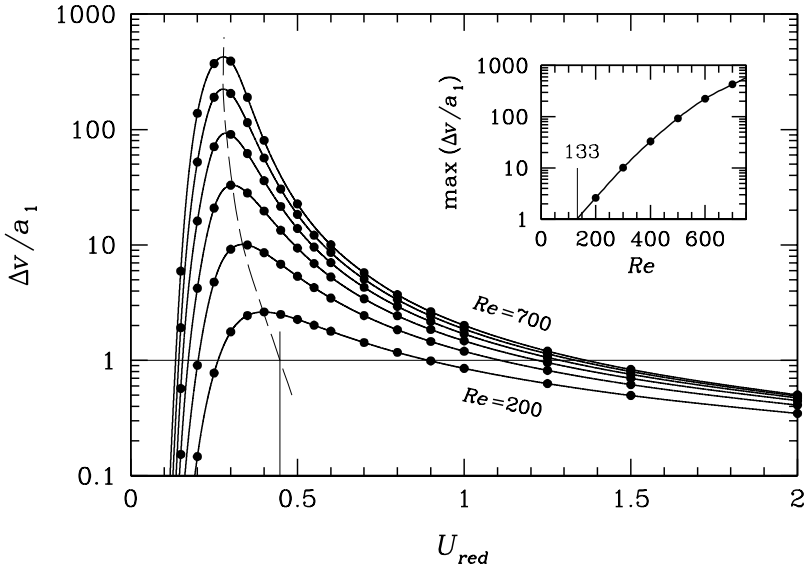

FIGURE 17. Convective instability results. These show the amplitude of radial velocity oscillation at ($z/D = 2.5$, $r/D = 0.25$), normalised by the amplitude of the streamwise velocity oscillation applied at the domain inlet. Inset shows the Re-dependence of the peak amplification.

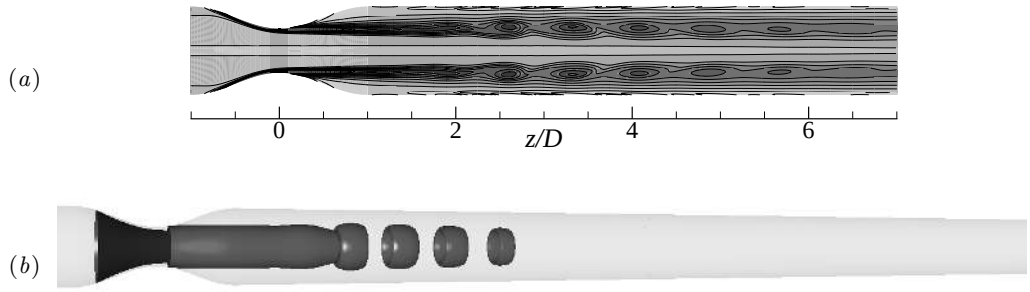

FIGURE 18. (a) Contours and (b) isosurface of instantaneous azimuthal vorticity for the axisymmetric convective instability of steady flow at $Re = 700$, $U_{red} = 0.3$, near peak sensitivity.

the stenosis, approximately in the centre of the shear layer. This is normalised by the magnitude of the perturbation, a_1, the quotient serving as a measure of amplification. The results of this analysis at normalised time periods in the region $0 \leq U_{red} \leq 2$ and for $200 \leqslant Re \leqslant 700$ are shown in figure 17. It can be seen that the shear layer is susceptible over a range of reduced velocites that broadens as Reynolds numbers increase, but also that the amplification becomes much more sharply peaked around a relatively narrow band of reduced velocities, $U_{red} \approx 0.28$ at $Re = 700$. It can be seen in the inset figure of peak amplification as a function of Reynolds number that the susceptibility also commences at quite low values, $Re \sim 133$.

In order to visualise this convective instability, we provide in figure 18 contours of the instantaneous axisymmetric azimuthal vorticity and an isosurface its three-dimensional projection for the flow at $U_{red} = 0.3$, $Re = 700$. Clearly, the shear layer is induced to roll up into a sequence of discrete ring vortices, although the process is not complete until approximately one diameter downstream of our sampling location at $z/D = 2.5$.

The mean vortex spacing at formation is $\Delta z/D \approx 0.7$, rising slowly downstream to approximately 0.8 before diffusion takes over and the vortices merge back into the mean shear layer at $z/D \sim 6$.

7. Discussion

Figure 19 (*a*) shows a compilation of the marginal stability curves for the wavy and period-doubling absolute instability modes, together with the envelope of $\Delta v/a_1 = 1$ and curve of peak amplification, $\max(\Delta v/a_1)$, for the convective shear layer instability. Figure 19 (*b*) re-presents the same data, but with Womersley number as the independent variable, rather than reduced velocity. We recall that the convective shear layer study was performed with a unsteady inflow component which was 1/1000th the amplitude of the mean flow (or 1/750th the amplitude of the oscillatory component of the pulsatile flows) and can be interpreted as a steady flow with comparatively high frequency, low amplitude noise. While the steady flow is not directly comparable to the two pulsatile cases, as a broad statement we can say that as the pulse period falls, the flow is first most susceptible to the period-doubling instability, then the wavy instability, and finally to high-frequency shear layer oscillations. Implicit in this statement is that the period-doubling and wavy instabilities do not have any noise present in the inflow since at high reduced velocity a quasi-steady flow is recovered and so the presence of high frequency noise would also be expected to drive shear layer instabilities. It is also possible that the axisymmetric shear-layer instability is in turn susceptible to still smaller-scale secondary three-dimensional instabilities, although we have not examined this aspect.

As we noted in § 1, the experimental observations and previous numerical studies are broadly consistent in predicting that when Reynolds numbers are high enough for transition to occur, this is manifested as pulse-locked turbulent bursts that are located some diameters downstream of the stenosis, and the flow then will relaminarise further downstream. Our present results support and extend those findings by showing a pulse-period dependence of the axial location of these turbulent bursts, brought about by self-destruction of vortex rings through either period-doubling or wavy instabilities. It is evident from an examination of figures 9 and 16 that the location of turbulent breakdowns in the asymptotic states moves downstream as reduced velocity, or equivalently pulse period, is increased. In fact, one might expect there to be a simple linear relationship between this location and the reduced velocity. In figure 20 we plot the axial location of the centroid of the distribution of q' (taken when the total turbulent kinetic energy is a maximum at one of the eight phase points) against reduced velocity, and it is seen that indeed such an approximately linear relationship exists.

In the larger arterial vessels of the human cardiovascular system, physiologically reasonable parameters can be argued to be in the range $100 \leqslant Re \leqslant 600$ and $4 \leqslant \alpha \leqslant 25$ in rest conditions (see e.g. McDonald 1974; Nichols & O'Rourke 1998). Since for a given pulse rate and blood viscosity, α increases directly with vessel diameter, large Womersley numbers are associated with the bigger vessels. Although conditions may change with pathology or with exertion, an examination of figure 19 (*b*) suggests that all of the instability modes examined here are directly relevant to human arterial flows where significant stenosis is present.

The flow rate waveforms observed in the human body cannot typically be represented by a single Fourier harmonic but may contain between eight to sixteen significantly energetic harmonics. The interaction between multiple harmonics is beyond the scope of this work. However, if for argument's sake we consider that the instabilities behave as a linear superposition, then a period doubling instability occuring at $Re = 400$, $U_{red} = 2.8$

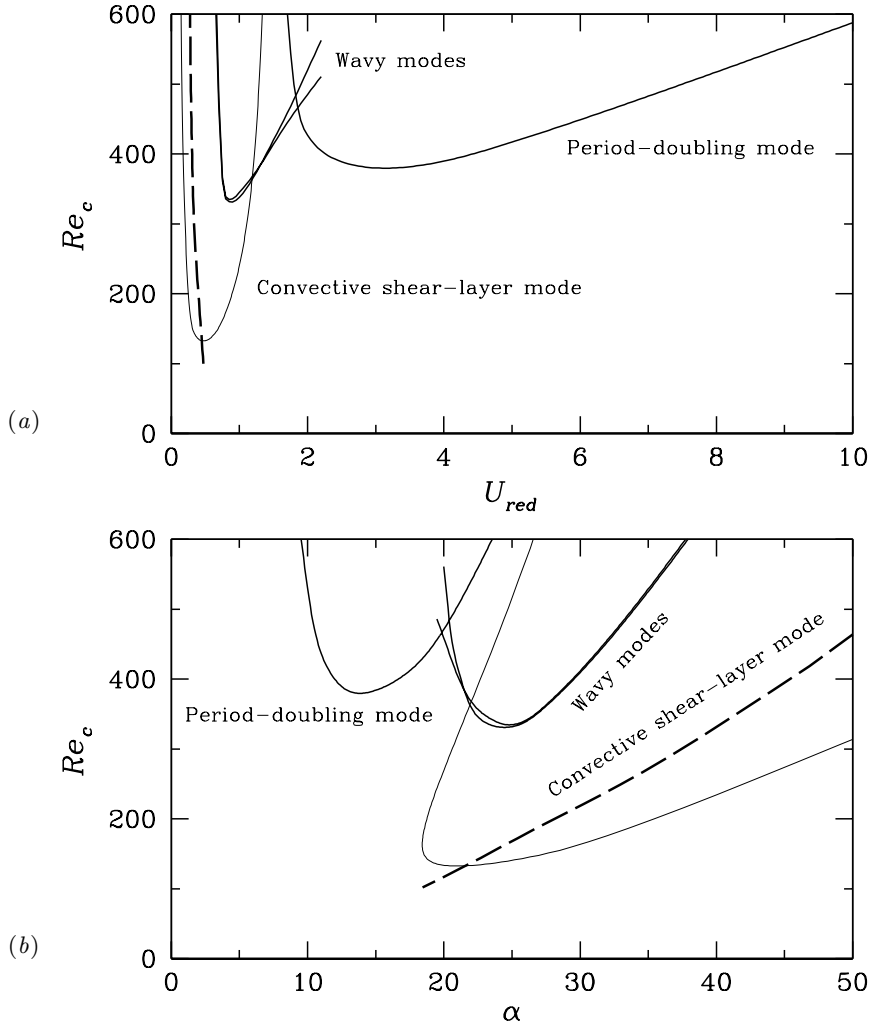

FIGURE 19. Summary of instability data, with Reynolds numbers plotted as functions of (*a*) reduced velocity and (*b*) Womersley number. For the wavy and period-doubling modes of the pulsatile flows, the curves of marginal stability are shown, while for the shear-layer instability of steady flow, the solid line is the contour of $\Delta v/a_1 = 1$ and the dashed line is the curve of peak amplification.

could be associated with an eighth-harmonic flow frequency which will have an effective reduced velocity of $U_{red} = 2.8/8 = 0.35$. This reduced velocity will then be close to the peak amplification of the shear layer instability. Our present results for the susceptibility to shear-layer instability of steady stenotic flow, together with our earlier study of shear-layer instability in a two-harmonic pulsatile flow (Sherwin & Blackburn 2005, § 6.4.3), and in vitro flow visualisations (Ahmed & Giddens 1983; Cassanova & Giddens 1978; Khalifa & Giddens 1981; Ojha *et al.* 1989), suggest that shear-layer oscillations (as opposed to turbulent breakdowns associated with vortex rings) may be common in these types of stenosis. Since shear layer instabilities are convective in nature and hence dependent on the magnitude and frequency content of any imposed disturbance (owing e.g. to vessel wall movement, upstream flow separation, respiratory or external body motion) it is

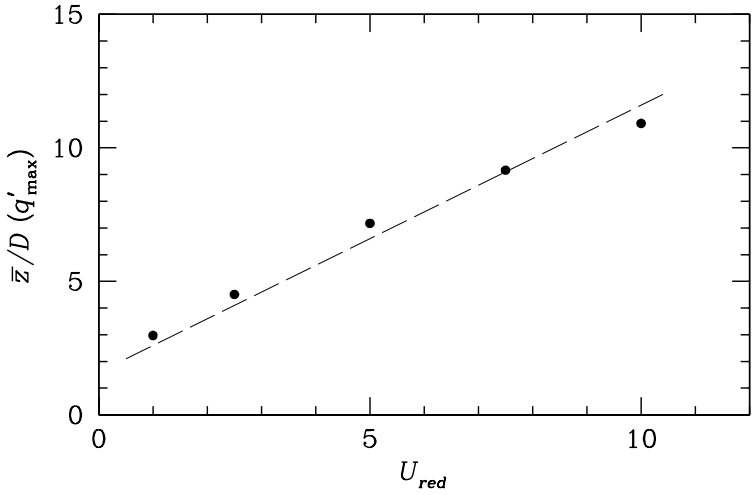

FIGURE 20. Axial location of the centroid of maximum turbulent energy (conditioned by phase averaging) in asymptotic states. The dashed line has a slope of unity.

very difficult to comment on their physiological importance relative to the vortex-ring instability mechanisms without further information.

It is not uncommon for atherosclerotic stenoses to be found not as isolated instances, but serially along an arterial branch (Goldstein, Demetriou, Grines, Pica & O'Neill 2000; Dodds & Phillips 2003). We may speculate that this pathology is somehow related to our observations of localised turbulent bursts downstream of a stenotic contraction, with associated high temporal and spatial gradients of shear stress on endothelial cells, while the magnitude of stress would be lower than that existing in the stenosis throat itself. If such a linkage exists, one might expect that multiple inline stenoses are created serially in time, too, with each successive stenosis helping to create fluid-mechanical conditions conducive to growth of a downstream plaque.

It is worth remarking that the instability modes we have noted in stenotic flow can be regarded as walled-bounded (but open) flow counterparts of previously recorded unbounded flow instabilities. The period-doubling mode seems closely related to the phenomenon of bifurcation of pulsed jet flows (Reynolds, Parekh, Juvet & Lee 2003), while the wavy mode appears closely related to the short-wave instability of isolated vortex rings (Widnall *et al.* 1974). The convective instability of (jet) shear layers has received extensive analytical treatment (see e.g. Monkewitz & Huerre 1982; Huerre & Rossi 1998), while plates 118–120 of Van Dyke (1982) provide a good visual adjunct to these theoretical works.

8. Conclusions

Through a systematic parametric variation of dimensionless pulse period for a simple pulsatile stenotic flow, we have shown that there are two kinds of absolute instability modes: a period-doubling mode that dominates at high reduced velocity, and a set of wavy modes that dominate at low reduced velocity. In addition, for steady flow the separated shear layer is susceptible to convective instability at still lower reduced velocities. With a more physiologically realistic flow waveform it is difficult to say in advance which of these might manifest themselves, either separately or in concert, and we plan to investigate this aspect in future work.

If Reynolds numbers are sufficiently high there will be a region of localised turbulent breakdown downstream of a stenotic contraction, followed by re-laminarisation. In our original problem definition we mentioned that adoption of a 75% stenosis is motivated by the observation that in clinical practice a blockage can be readily identified through medical imaging as it corresponds to a 50% reduction in arterial diameter. The current investigation has further determined that for this degree of stenosis, transitional flow leading to a turbulent breakdown is possible at physiologically relevant values of Reynolds number and non-dimensional pulse period.

While in real physiological flows geometric imperfections such as stenosis asymmetry and vessel curvature, along with vessel distensibility, will play a role in determining the nature of transition, our present work does not examine these aspects, but is intended to serve as a point of reference for such studies.

This work was supported through the Merit Allocation Scheme of the Australian Partnership for Advanced Computing, and all three-dimensional DNS studies were computed at APAC's National Facility in Canberra, to whose staff we extend our thanks. H. M. B. wishes to acknowledge EPSRC grant GR/T02553/01 in financial support of a Visiting Fellowship. S. J. S. would like to acknowledge financial support from the Royal Academy of Engineering in the form of a Global Research Award.

REFERENCES

Ahmed, S. A. 1998 An experimental investigation of pulsatile flow through a smooth constriction. *Exptl Thermal & Fluid Sci.* **17**, 309–318.

Ahmed, S. A. & Giddens, D. P. 1983 Velocity measurements in steady flow through axisymmetric stenoses at moderate reynolds numbers. *J. Biomechanics* **16** (7), 505–516.

Ahmed, S. A. & Giddens, D. P. 1984 Pulsatile poststenotic flow studies with laser Doppler anemometry. *J. Biomechanics* **17** (9), 695–705.

Akhavan, R., Kamm, R. D. & Shapiro, A. H. 1991 An investigation of transition to turbulence in bounded oscillatory Stokes flows Part 1. Experiments. *J. Fluid Mech.* **225**, 395–422.

Berger, S. A. & Jou, L.-D. 2000 Flows in stenotic vessels. *Annu. Rev. Fluid Mech.* **32**, 347–384.

Blackburn, H. M. 2002 Three-dimensional instability and state selection in an oscillatory axisymmetric swirling flow. *Phys. Fluids* **14** (11), 3983–3996.

Blackburn, H. M., Mansour, N. N. & Cantwell, B. J. 1996 Topology of fine-scale motions in turbulent channel flow. *J. Fluid Mech.* **310**, 269–292.

Blackburn, H. M. & Sherwin, S. J. 2004 Formulation of a Galerkin spectral element–Fourier method for three-dimensional incompressible flows in cylindrical geometries. *J. Comput. Phys.* **197** (2), 759–778.

Caro, C. G., Fitz-Gerald, J. M. & Schroter, R. C. 1971 Atheroma and arterial wall shear: Observation, correlation and proposal of a shear dependent mass transfer mechanism for atherogenesis. *Proc. Roy. Soc. Lond. B* **177**, 109–159.

Cassanova, R. A. & Giddens, D. P. 1978 Disorder distal to modified stenoses in steady and pulsatile flow. *J. Biomechanics* **11**, 441–453.

Dodds, S. R. & Phillips, P. S. 2003 The haemodynamics of multiple sequential stenoses and the criteria for a critical stenosis. *Eur. J. Endovasc. Surg.* **26**, 348–353.

Gharib, M., Rambod, E. & Shariff, K. 1998 A universal time scale for vortex ring formation. *J. Fluid Mech.* **360**, 121–140.

Goldstein, J. A., Demetriou, D., Grines, C., Pica, M. & O'Neill, W. W. 2000 Multiple complex coronary plaques in patients with acute myocardial infarction. *New England Journal of Medicine* **343** (13), 915–922.

Huerre, P. & Rossi, M. 1998 Hydrodynamic instabilities in open flows. In *Hydrodynamics and Nonlinear Instabilities* (ed. C. Godrèche & P. Manneville), pp. 81–294. Cambridge University Press.

Khalifa, A. M. A. & Giddens, D. P. 1981 Characterization and evolution of poststenotic disturbances. *J. Biomechanics* **14** (5), 279–296.

Ku, D. N. 1997 Blood flow in arteries. *Annu. Rev. Fluid Mech.* **29**, 399–434.

Long, Q., Xu, X. Y., Ramnarine, K. V. & Hoskins, P. 2001 Numerical investigation of physiologically realistic pulsatile flow through arterial stenosis. *J. Biomechanics* **34**, 1229–1242.

Mallinger, F. & Drikakis, D. 2002 Instability in three-dimensional, unsteady, stenotic flows. *Intnl J. Heat Fluid Flow* **23**, 657–663.

McDonald, D. A. 1974 *Blood Flow in Arteries*, 2nd edn. Edward Arnold.

Mittal, R., Simmons, S. & Najjar, F. 2003 Numerical study of pulsatile flow in a constricted channel. *J. Fluid Mech.* **485**, 337–378.

Monkewitz, P. A. & Huerre, P. 1982 Influence of the velocity ratio on the spatial instability of mixing layers. *Phys. Fluids* **25** (7), 1137–1143.

Nichols, W. W. & O'Rourke, M. F. 1998 *McDonald's Blood Flow in Arteries: Theoretical, Experimental and Clinical Principles*, 4th edn. London: Arnold.

Ojha, M., Cobbold, R. S. C., Johnston, K. W. & Hummel, R. L. 1989 Pulsatile flow through constricted tubes: An experimental investigation using photochromic tracer methods. *J. Fluid Mech.* **203**, 173–197.

Pedley, T. J. 2000 Blood flow in arteries and veins. In *Perspectives in Fluid Dynamics: A Collective Introduction to Current Research* (ed. G. K. Batchelor, H. K. Moffatt & M. G. Worster), chap. 3, pp. 105–158. Cambridge University Press.

Pitt, R., Sherwin, S. J. & Theofilis, V. 2005 Biglobal stability analysis of steady flow in constricted channel geometries. *Intnl J. Num. Meth. Fluids* **47** (10-11), 1227–1235.

Reynolds, W. C. & Hussain, A. K. M. F. 1972 The mechanics of an organized wave in turbulent shear flow. Part 3. Theoretical models and comparisons with experiments. *J. Fluid Mech.* **41** (263–288).

Reynolds, W. C., Parekh, D. E., Juvet, P. J. D. & Lee, M. J. D. 2003 Bifurcating and blooming jets. *Annu. Rev. Fluid Mech.* **35**, 295–315.

Rosenfeld, M., Rambod, E. & Gharib, M. 1998 Circulation and formation number of laminar vortex rings. *J. Fluid Mech.* **376**, 297–318.

Sherwin, S. J. & Blackburn, H. M. 2005 Three-dimensional instabilities and transition of steady and pulsatile flows in an axisymmetric stenotic tube. *J. Fluid Mech.* **533**, 297–327.

Sobey, I. J. & Drazin, P. G. 86 Bifurcations of two-dimensional channel flows. *J. Fluid Mech.* **171**, 263–287.

Stroud, J. S., Berger, S. A. & Saloner, D. 2000 Influence of stenosis morphology on flow through stenotic vessels: implications for plaque rupture. *J. Biomechanics* **33**, 443–455.

Stroud, J. S., Berger, S. A. & Saloner, D. 2002 Numerical analysis of flow through a severely stenotic carotid artery bifurcation. *ASME J. Biomech. Eng.* **124**, 9–20.

Taylor, C. A. & Draney, M. L. 2004 Experimental and computational methods in cardiovascular fluid mechanics. *Annu. Rev. Fluid Mech.* **36**, 197–231.

Van Dyke, M. 1982 *An Album of Fluid Motion*. Stanford, CA: Parabolic Press.

Varghese, S., Frankel, S. & Fischer, P. 2005 Direct numerical simulation of stenotic flow. Part 2. Pulsatile flow. *J. Fluid Mech.* Submitted.

Widnall, S. E., Bliss, D. B. & Tsai, C.-Y. 1974 The instability of short waves on a vortex ring. *J. Fluid Mech.* **66** (1), 35–47.

Womersley, J. R. 1955 Method for the calculation of velocity, rate of flow and viscous drag in arteries when the pressure gradient is known. *J. Physiology* **127**, 553–563.

Wootton, D. M. & Ku, D. N. 1999 Fluid mechanics of vascular systems, diseases, and thrombosis. *Annu. Rev. Biomed. Eng.* **1**, 299–329.

Yang, W. H. & Yih, C.-S. 1977 Stability of time-periodic flows in a circular pipe. *J. Fluid Mech.* **82**, 497–505.